Na^+ Ion Mobility in $Na_{3+x}Sc_2(SiO_4)_x(PO_4)_{3-x}$ ($0.1 < x < 0.8$) Observed by ^{23}Na NMR Spectroscopy

Tatiana Zinkevich[1,2], Andy Fiedler[1], Marie Guin[3,4,*], Frank Tietz[3,4], Olivier Guillon[3,4,5], Helmut Ehrenberg[1,2], Sylvio Indris[1,2]

[1]Institute for Applied Materials – Energy Storage Systems (IAM-ESS), Karlsruhe Institute of Technology (KIT), Hermann-von-Helmholtz-Platz 1, 76344 Eggenstein-Leopoldshafen, Germany

[2]Helmholtz Institute Ulm, Helmholtzstraße 11, 89081 Ulm, Germany

[3]Institute of Energy and Climate Research, Materials Synthesis and Processing (IEK-1), Forschungszentrum Jülich GmbH, 52425 Jülich, Germany

[4]Helmholtz Institute Münster, Forschungszentrum Jülich GmbH, D-52425 Jülich, Germany

[5]Jülich Aachen Research Alliance, JARA-Energy

*present address: Saint Gobain Sekurit GmbH & Co. KG, Chemical Labs, Glasstr. 1, 52134 Herzogenrath, Germany

Abstract

The mobility of Na^+ ions in $Na_{3+x}Sc_2(SiO_4)_x(PO_4)_{3-x}$ ($0.1 < x < 0.8$) was investigated by temperature-dependent ^{23}Na NMR spectroscopy and relaxometry. These measurements are probing the local motion of the Na^+ ions and give information about the average hopping rate of the ions and the activation barriers these ions have to overcome for single jumps. The results are compared with those obtained by impedance spectroscopy that is probing the long-range transport of the Na^+ ions. A consistent picture is obtained with the fastest motion of the Na^+ ions observed for the sample with x = 0.4.

1. Introduction

Recently all-solid-state batteries have attracted a lot of attention because of their possibly enhanced safety properties. In contrast to liquid electrolytes, solid electrolytes are leak-proof and non-flammable. In such conductors, Li^+ ions are mostly used as charge carriers due to their high accessible operating voltage in the battery and thus high energy density. However, Na-based conductive materials represent an alternative for a future design of batteries. The raw materials for these solids are highly abundant, inexpensive, environmentally friendly, and non-toxic. Although Na^+-based electrolytes are still less intensively investigated than the Li^+ counterparts, some materials can easily compete with common Li solid electrolytes in terms of ionic conductivity and economical relevance.

During the past decade NASICON-type structures have shown to exhibit high sodium conductivity reaching values of $5 \cdot 10^{-4}$ to $5 \cdot 10^{-3}$ S/cm at room temperature.(1–3) However, thiese values are still below the conductivity of liquid electrolytes and it is challenging to estimate the future progress in the development of even better conductive materials. This paper focuses on the characterization of a set of NASICON-type electrolytes with the common chemical formula $Na_{3+x}Sc_2(SiO_4)_x(PO_4)_{3-x}$ (hereafter named $NSSi_xP$), where *x* is in the range from 0.1 to 0.8. $NSSi_xP$ crystallizes in a rhombohedral structure with space group $R\bar{3}c$ (Figure 1a). PO_4 tetrahedra share common corners with ScO_6 octahedra forming an open network structure. Sodium ions were found to occupy three different positions in this structure and the conductivity pathway includes jumps between the Na(1) and Na(2)/Na(3) sites.(4,5) In order to perform a translational motion, Na^+ ions have to pass through two oxygen triangles which form a bottleneck for the Na mobility. These triangles are formed by oxygen ions on *6b* and *18e* sites and are named T1 and T2 (Figure 1b).

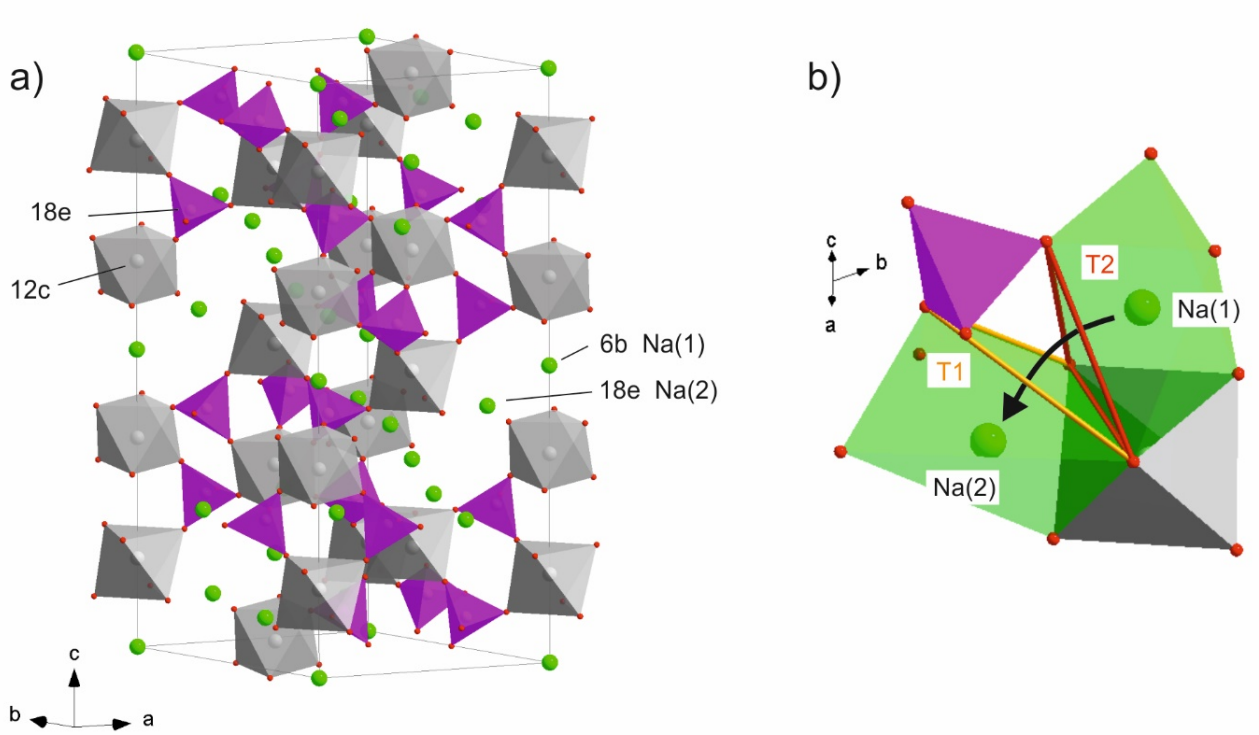

Figure 1 *a) The rhombohedral crystal structure of* $Na_{3+x}Sc_2(SiO_4)_x(PO_4)_{3-x}$ *with space group* $R\bar{3}c$. *b) the jump of* Na^+ *ions between the Na(1) and Na(2) sites through the oxygen triangles T1 and T2.*

The highest conductivity was obtained for x = 0.4 and reached a value of $\sigma = 6.9 \cdot 10^{-4}$ S/cm at 25 °C.(4) These materials are resistant against H_2O and CO_2 uptake in a wide temperature range,(6) and such a stability is of key importance for industrial purposes. Although several papers already report on the structural properties of the material, only limited data is available on the sodium ion mobility at the micro-scale. With this study we intend to cover this gap and derive a detailed picture of the Na motions with the help of solid-state NMR spectroscopy.

Solid-state NMR spectroscopy offers a variety of techniques to examine both the structure and dynamics in condensed matter.(7) Among these techniques, magic-angle spinning (MAS) multinuclear NMR spectroscopy is a well-known method to reveal the local environment around different probe nuclei and thus around specific elements/isotopes. The motional narrowing as detected by acquisition of temperature-dependent static ^{23}Na NMR spectra provides the activation energy for slow motions (on timescales of the order of some ms) which lead to averaging of anisotropic NMR interactions (dipolar and quadrupolar couplings and chemical shift anisotropy). Temperature-dependent spin-lattice relaxation rates are sensitive

to nanosecond dynamics and give activation energies and the timescales of corresponding motional processes.

The combination of NMR techniques revealing both structural and dynamic properties allows to investigate peculiarities of the Na^+ ion mobility and to correlate it with structural features and with results of impedance spectroscopy, X-ray diffraction, and neutron scattering.(4,5) A deeper understanding of the factors which influence the performance of electrolytes on a microscopic scale may allow to derive some rules for the rational design of conducting materials for all-solid-state batteries.

2. Materials and methods

2.1 Sample preparation

A conventional solid-state reaction was used to synthesize $Na_{3+x}Sc_2(SiO_4)_x(PO_4)_{3-x}$ samples. The starting materials were purchased from Merck KGaA ($NH_4H_2PO_4$), Projector GmbH (Sc_2O_3) and, Alfa Aesar GmbH & Co KG (Na_2CO_3 and SiO_2). A stoichiometric homogenized mixture of these materials was heated to 1173 K for 4 h. After subsequent milling, resulting powders were heated again to 1573 K for 20 h. Finally, powder samples were stored at ambient conditions.(4)

2.2 Experimental details

2.2.1 NMR spectroscopy

Multinuclear MAS NMR experiments were carried out at room temperature on a Bruker Avance 500 MHz spectrometer. Spinning was performed with 2.5 mm rotors at 30 kHz. ^{23}Na, ^{31}P, and ^{45}Sc NMR spectra were measured with a rotor-synchronized Hahn-echo pulse sequence. For the ^{31}P NMR spectra, the $\pi/2$ pulse length was 2.75 μs, the recycle delay was 100 s and the number of acquisitions was 64. The pulse length for ^{23}Na and ^{45}Sc was 1.6 μs and 1 μs and the recycle delay was 3.5 s and 60 s, respectively. The number of acquisitions was varied between 512-1024 scans. ^{29}Si NMR spectra were measured with a single-pulse sequence, a

$\pi/2$ pulse length of 1.8 μs, and a recycle delay of 60 s. The chemical shifts were referenced to an aqueous 1M NaCl solution for ^{23}Na (0 ppm), an aqueous 1M $ScCl_3$ solution for ^{45}Sc (0 ppm), a 85% solution of H_3PO_4 for ^{31}P (0 ppm), and tetramethyl silane for ^{29}Si (0 ppm). Temperature-dependent static ^{23}Na NMR measurements were performed on a Bruker Avance 200 MHz spectrometer at a magnetic field of 4.7 T, corresponding to a Larmor frequency of 52.9 MHz for ^{23}Na. Static ^{23}Na NMR spectra were acquired with a quadrupolar-echo pulse sequence and a $\pi/2$ pulse length between 10 and 12 μs. T_1 measurements were accomplished with an inversion-recovery pulse sequence with relaxation delays varying between 10 μs and 15 s. Up to 40 points have been measured for each magnetization transient. Two exponential functions were used to describe the magnetization transients. Since the relative intensity of the slower relaxing component was only 2-5%, it was neglected in the further data analysis. Additionally, a stretching factor (β) was used for the accurate description of the experimental data. The stretching factor for all samples, except for that with x = 0.1, was found to be approximately 0.4-0.7 for all temperatures. For x = 0.1, β was lower and varied between 0.2-0.4.

2.2.2 Raman spectroscopy

Raman spectra were recorded on a Horiba Evolution confocal microscope (Jobin-Yvon, France). The Raman spectrometer was equipped with a 50x long-working-distance objective with a numeric aperture of 0.9 and a 600-line grating. The excitation line was 532 nm from a Nd:YAG solid state laser with a power of 10 mW.

2.2.3 X-ray diffraction

The purity of the $NSSi_xP$ powders was investigated by X-ray diffraction (XRD) (Bruker D4 ENDEAVOR diffractometer, Cu Kα radiation). The powder patterns were analyzed by Rietveld refinements using the Jana program(9) to determine lattice parameters, atomic positions and site occupancies as already reported.(4)

3. Results and Discussions

3.1 Structural characterization

3.1.1 X-ray diffraction

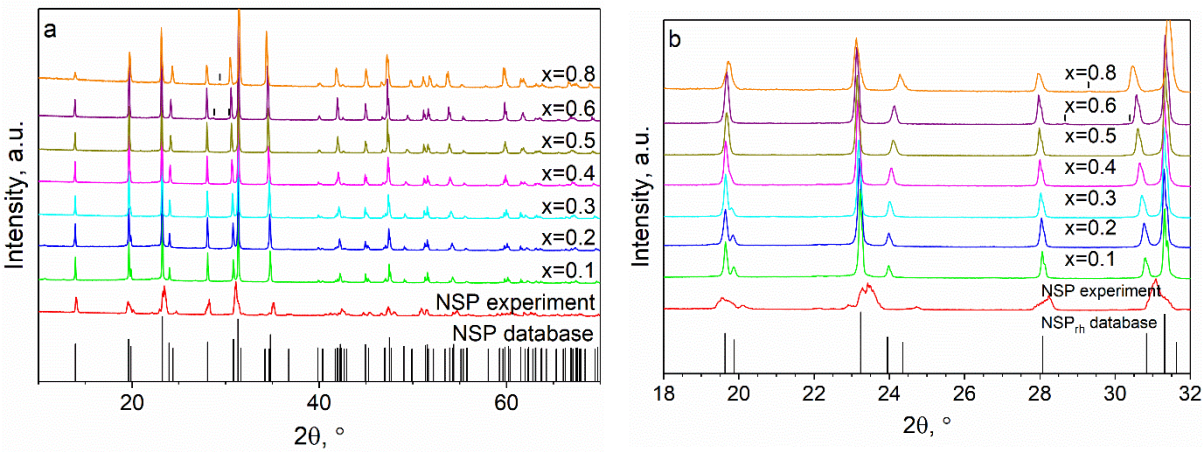

Figure 2 XRD patterns of the $NSSi_xP$ samples: (a) full patterns and (b) magnified view of the range 18-32°. The monoclinic reference sample $Na_3Sc_2P_3O_{12}$ (NSP) is shown for comparison together with the ICSD database pattern (ref. no. 01-079-0480). The vertical tick marks shown for the x=0.6 and x=0.8 sample represent minor, unidentified impurities.

Figure 2 displays the XRD patterns for the series of samples with increasing Si content. All these patterns are characteristic of the NASICON structure, but in some cases small reflections were observed in addition to the main phase (these are denoted with vertical black lines for samples with x=0.6 and x=0.8), indicating the existence of small amounts of impurity phases which do not exceed 3% of the total weight fraction. Due to the low intensity of the signals of impurities, an assignment was not possible. Additionally, the pattern of a sample with x = 0, $Na_3Sc_2(PO_4)_3$, is presented in the figure. The structure of this sample is monoclinic which is in

agreement with the database pattern. However, small, unidentified impurities are also visible for this sample.

For all samples with x > 0 the rhombohedral structure was detected from the characteristic single reflection at 2θ = 28° whereas in the case of a monoclinic arrangement a splitting of this peak appears, as can be seen in the pattern measured for the sample with *x* = 0 (Figure 2).

3.1.2 Raman spectroscopy

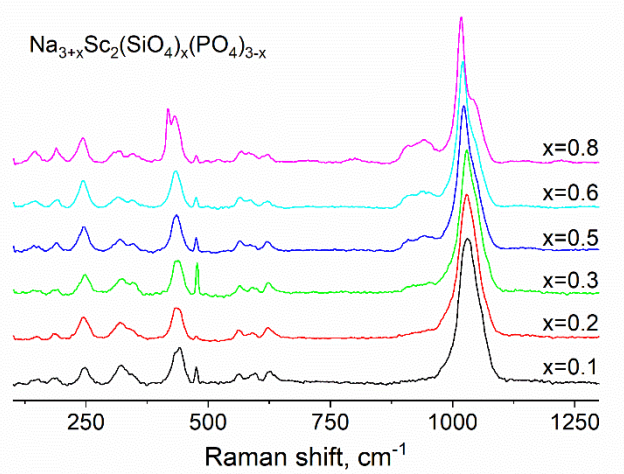

Figure 3 Raman spectra of $NSSi_xP$ with *x* ranging between 0.1 and 0.8.

The Raman spectra of $Na_{3+x}Sc_2(SiO_4)_x(PO_4)_{3-x}$ are presented in Figure 3. Different peaks are visible which represent vibrations of PO_4 and SiO_4 groups. The most intense broad line is located at around 1050 cm^{-1}. The absence of a clear fine structure is consistent with a rhombohedral arrangement,(10) which is in line with the XRD results described above. With a gradual increase of the Si content, a shoulder becomes apparent on the right side of this peak due to progressive line narrowing. Line broadening at lower sodium fractions in NASICON samples was previously attributed to short-range disorder,(11,12) which is originating from partial occupation of the Na(1) position. The vacancies at these sites cause distortions of the PO_4/SiO_4 tetrahedra, which are reflected by the position of the peaks. With increasing sodium content more and more Na(1) sites are occupied(4) and, thus, the distribution of local environments narrows. Both contributions of the broad signal slightly change their positions as

a function of *x*. This fact may be explained by an increasing silicon fraction and a decreasing phosphorous fraction. The SiO_4 ν_3-mode at about 1000 cm^{-1} slightly shifts towards lower wavenumbers as compared to PO_4(11) and both vibrations are entangled resulting in a common peak.(13,14) The changes with increasing *x* are not only visible in the broad signal at 1050 cm^{-1}. In addition, a gradual increase of the intensity in the range of 881-971 cm^{-1} can be identified from the figure. This feature is generated by intramolecular stretching vibrations in SiO_4,(11) and its intensity accordingly increases with increasing Si content.

Furthermore, a series of bands is visible at 500-700 cm^{-1}. These signals are related to the antisymmetric and symmetric bending modes of both SiO_4 and PO_4(15–17) which are hard to detangle, while the peaks at <400 cm^{-1} result from external modes and represent different motions of the PO_4 and SiO_4 tetrahedra.(10,15) The presence of some minor phases was also observed by Raman spectroscopy. For example, a peak at 475 cm^{-1}, which is apparent for all

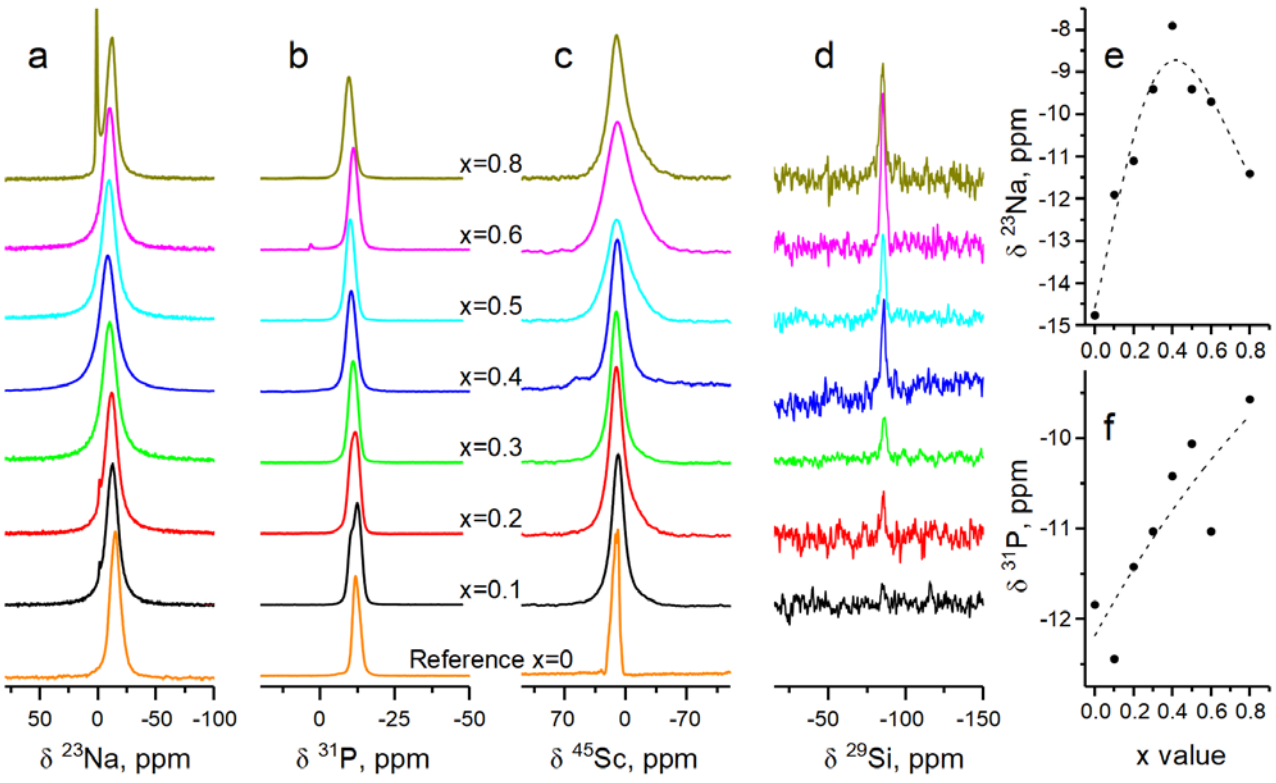

Figure 4 (a) ^{23}Na, (b) ^{31}P, (c) ^{45}Sc and (d) ^{29}Si MAS NMR spectra and the change of the (e) ^{23}Na and (f) ^{31}P chemical shift as a function of Si content *x*.

the samples, could not be assigned to the main phase, as well as another one at 417 cm^{-1} existing for the sample with x = 0.8.

3.1.2 Magic-angle spinning NMR spectroscopy

Figure 4a-d present ^{23}Na, ^{31}P, ^{45}Sc, and ^{29}Si MAS NMR spectra for the series of $NSSi_xP$ samples. As can be seen from Figure 4a, the most notable difference between the different ^{23}Na NMR spectra is the appearance of a narrow signal at approximately 0 ppm, which is very intense for x = 0.8. Taking into account the chemical shift value for this narrow signal we can deduce the existence of sodium (hydro)-carbonate,(18,19) which could appear due to the excess of sodium and its interaction with air.

As it is expected from the $NSSi_xP$ structure, at least two different sites for the Na ions should be visible in the ^{23}Na NMR spectra, Na(1) and Na(2)/Na(3) (there is a fast exchange between Na(2) and Na(3) and, thus, the latter might be represented by a single line). In fact, there are even more chemically non-equivalent environments around Na due to the different next-nearest neighbours. Each Na^+ ion is surrounded by six oxygen ions, which are linked to either Si or P atoms. If the SiO_4 and PO_4 tetrahedra are distributed randomly, there is a whole set of different combinations of next-nearest neighbours around sodium giving rise to several resonance frequencies. Moreover, a line broadening due to strong quadrupolar coupling inducing fast transverse relaxation further complicates the analysis. Another possible reason for the existence of just one broad peak is the fast exchange between the different Na sites in the structure, which can be expected from the high ionic conductivity in these materials. As a result, peak deconvolution is not possible and only the single broad peak is visible which comprises overlapping signals from different sodium sites and environments.

With increasing Si content, more and more PO_4 tetrahedra are substituted by SiO_4. This fact results in the change of the isotropic chemical shift of the sodium spectra. The maximum of the peak shifts towards more positive values as x increases, reaches its maximum for $x \approx 0.5$, and then slightly moves back (see Figure 4e). Also the peak width changes with x. Initially the width increases with x until x = 0.4 and then it decreases again. This behavior reflects the

altered distribution of local environments around the sodium sites. Two different effects may contribute to the overall changes in the linewidth: *(i)* the increase of the silicon content leads to a distortion of the symmetry around sodium sites and *(ii)* the structure becomes saturated with Na^+ ions which reduces the number of vacancies and induces more order as was reported earlier.(11) The transverse relaxation also changes with increasing content of Na due to stronger quadrupolar coupling.(20,21) This effect of line broadening might not be fully suppressed in the MAS NMR spectra.

The ^{31}P NMR spectra consist of a central line with no spinning sidebands due to the low interaction anisotropy. For $x = 0.1$ two contributions to the overall signal can be identified. The shoulder at the left side of the spectrum may hint at the presence of a small amount of $Na_3Sc_2(PO_4)_3$, as can be seen by comparison of this spectrum with that of the sample with x = 0. With increasing amount of SiO_4 tetrahedra the second signal disappears and a single resonance is obtained. The position of the central line shifts towards higher frequencies as *x* increases, due to the weaker electronegativity of the Si atoms. Figure 4e and 4f summarize the variation of the ^{31}P and ^{23}Na isotropic chemical shifts as a function of the material composition. A shift of the ^{23}Na peak to lower frequencies can be explained by different electronegativities of the Si and P atoms.(22) Phosphorous substitution with Si atoms leads to a charge redistribution which in turn changes the chemical shielding of the nucleus under study. A shift of the sodium resonance to more positive values at higher Si contents might be attributed to the saturation of the crystal with sodium ions, which changes the charge distribution and influences the ^{23}Na chemical shift. These results are in good agreement with previous investigations on $Na_{1+x}Zr_2(SiO_4)_x(PO_4)_{3-x}$.(22)

The ^{45}Sc NMR spectra of the samples with $x > 0.1$ (Figure 4c) show a single broad resonance at 16.4 ppm and a gradual line broadening with increasing *x* whereas the position of this peak stays constant. For $x = 0$, the Sc ions are surrounded exclusively by PO_4 groups and the spectrum reveals a single resonance at 11 ppm with residual quadrupolar coupling. The different chemical shift for this sample can be explained by the different crystal structure and thus a different local environment around Sc. As PO_4 is successively substituted by SiO_4, a

variety of local environments occurs around the Sc giving rise to multiple overlapping peaks and thus to a broader line, as can be seen especially for x > 0.5.

The ^{29}Si NMR spectra (Figure 4d) show a single peak at -85 ppm which represents [SiO_4] units with four bridging oxygen ions, as expected from the crystal structure. The intensity of this line is increasing with *x* reflecting the increasing silicon content.

3.2 Na^+ ion dynamics

3.2.1 ^{23}Na NMR lineshape and motional narrowing

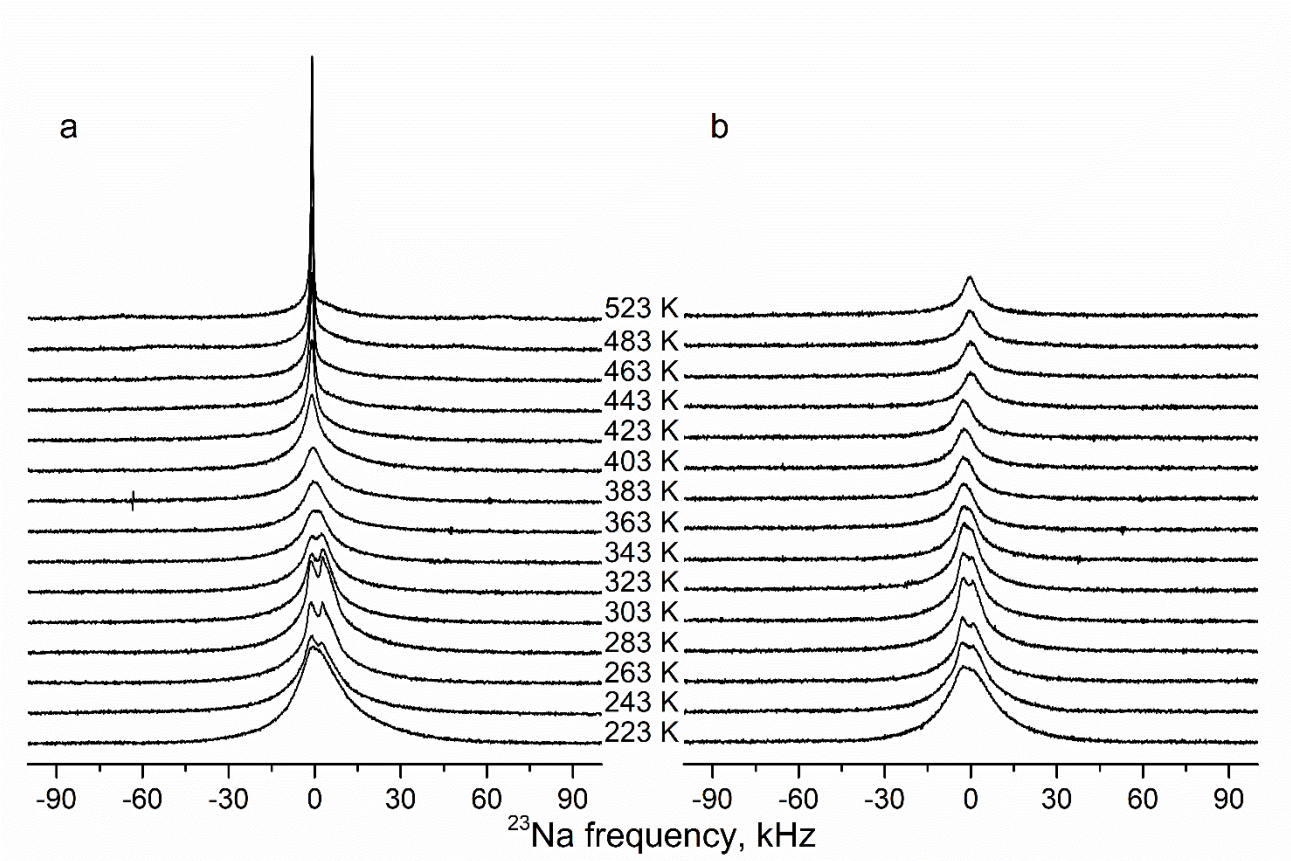

Figure 5 Static ^{23}Na spectra for (a) $NSSi_{0.1}P$ and (b) $NSSi_{0.8}P$ for temperatures between 223 K and 523 K.

The temperature-dependent quadrupolar echo experiment is a tool to characterize motional processes which occur on millisecond timescales. Motions occurring on these time sclaes lead to the gradual narrowing of the central transition which is significantly broadened at the “rigid-lattice” limit (at low temperatures) due to the dipolar interaction as well as chemical shift

anisotropy. Upon temperature increase, faster motion of the Na^+ ions and thus of the Na nuclei averages the distribution of these interactions and a narrowed signal appears. This effect can be seen in Figure 5a, which represents the motional narrowing effect exemplarily for $Na_{3.1}Sc_2(SiO_4)_{0.1}(PO_4)_{2.9}$ and $Na_{3.8}Sc_2(SiO_4)_{0.8}(PO_4)_{2.2}$. At the lowest temperature of 223 K an asymmetric broad featureless line was observed. Due to the narrowing effect this line splits into two separate signals in the temperature range of 243-303 K. The splitting is assigned to the residual quadrupolar coupling. Another source of the signal splitting might be a slight difference in chemical shifts. However, since both signals revealed a similar relaxation behavior, this possibility was excluded. The existence of only one broad peak in the ^{23}Na MAS NMR spectrum (Figure 4a) further supports the assumption of quadrupolar-coupling caused splitting in the static ^{23}Na NMR spectrum. For higher temperatures, the temperature-induced enhancement of the mobility causes a gradual narrowing of the signal until its width reaches the “mobile” limit. Then the width of the signal is mainly originating from the magnetic field inhomogeneity. A similar behavior has been observed earlier for the sample with x = 0.4.(23)

In summary, if the linewidth is measured as a function of temperature in a large temperature range, the curve consists of three distinct regions: *(i)* a flat plateau at low temperatures which corresponds to the rigid-lattice limit and is characterized by the structural features of the material, *(ii)* a temperature-induced gradual reduction of the width, which starts if the motional rate reaches the low-temperature width of the signal, and *(iii)* the high-temperature plateau where all motions are fast and only the field inhomogeneity contributes to the line width. In the case when all regions are accessible, it is possible to estimate the activation energy E_a of the motion from the experimentally measured onset of the narrowing. There are several ways to quantify experimental results, and one of them is the phenomenological approach formulated by Hendrickson-Bray:(24)

$$\Delta\upsilon(T) = \Delta\upsilon_{\mathrm{R}}\left[1 + \left(\frac{\Delta\upsilon_{\mathrm{R}}}{B} - 1\right)\cdot \exp\left(-\frac{E_{\mathrm{a}}}{k_{\mathrm{B}}T}\right)\right]^{-1} + D \qquad \text{Equation 1}$$

Here $\Delta\upsilon(T)$ denotes the linewidth of the central transition at temperature T, D is the high-temperature plateau value, $\Delta\upsilon_{\mathrm{R}}$ includes the linewidth of the rigid lattice, B is attributed to the linewidth of the thermally activated nuclei, and k_{B} is the Boltzmann constant.

The temperature dependence of the linewidth for different $NSSi_xP$ samples is depicted in Figure 6 along with fitted curves according to Eq. (1). In order to discard any uncertainty due to the quadrupolar splitting, only the temperature range was analyzed where just a single peak appeared. Since a clear plateau cannot be observed within the accessible temperature range, only rough estimations about the dynamics can be made from these data. The red lines in Figure 6 correspond to the fitting according to this Hendrickson-Bray approach (Eq. (1)). Since the "completely narrowed" regime was not reached for some samples, the *D* parameter can be fitted only with a certain degree of inaccuracy. Assuming that the field inhomogeneity stays the same for the whole set of samples, we fixed the *D* parameter based on the value obtained for the first sample (*D* = 0.65 kHz).

The composition of the sample strongly influences the behavior of these curves. At the lowest silicon content, a clear step is visible with both high-temperature and low-temperature plateaus. With increasing *x*, a smoother reduction of the linewidth occurs with increasing temperature. At *x* = 0.6 neither rigid-lattice nor mobile-limit plateaus are apparent and almost all data points are located in the sloping region. This is even more pronounced for the last sample $NSSi_{0.8}P$. Here, only a small segment of the sloping region was measured within the accessible temperature range. Therefore, a fitting of the line width was not possible for this sample and the grey dashed line in Fig. 6 is just given to guide the eye. The fit parameters for the other samples are summarized in Table 1.

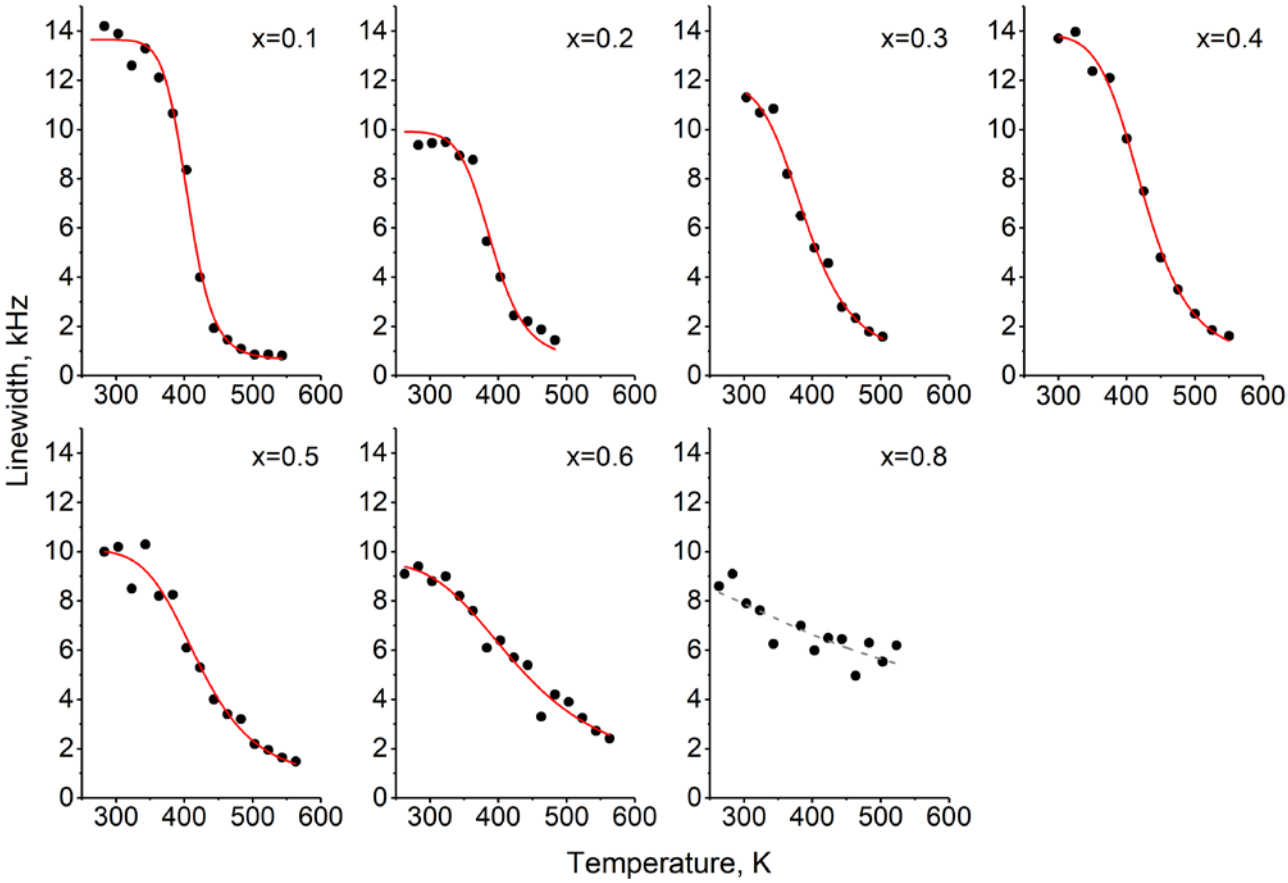

Figure 6 The linewidth of the central transition in the ^{23}Na static spectra as a function of temperature. The experimental linewidths (black points) are obtained as the full width at half maximum. The red lines represent the fits according to the phenomenological approach described in Ref [20]. The grey dashed line for x=0.8 is just a guide to the eye.

Table 1 Fitting parameters for the temperature-dependent linewidth.

x	$\Delta\upsilon_R$, kHz	B, kHz	E_a, eV
0.1	13.0 ± 0.5	$3.6\cdot10^{-9}$	0.73 ± 0.18
0.2	9.3 ± 0.3	$1.2\cdot10^{-6}$	0.51 ± 0.09
0.3	11.3 ± 0.5	$1.5\cdot10^{-4}$	0.36 ± 0.04
0.4	13.2 ± 0.2	$6\cdot10^{-5}$	0.43 ± 0.03
0.5	9.4 ± 0.4	$4.5\cdot10^{-4}$	0.34 ± 0.04
0.6	8.9 ± 0.4	$2.6\cdot10^{-2}$	0.21 ± 0.03

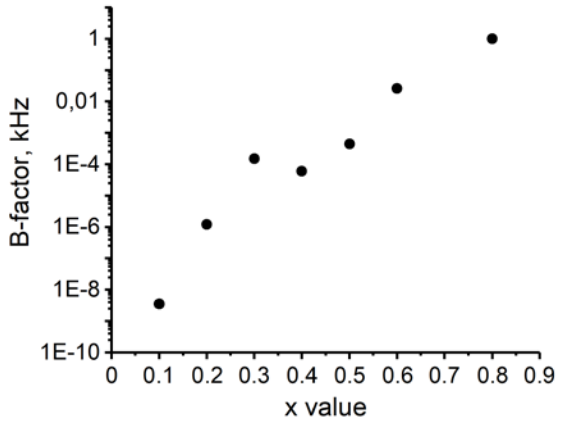

Figure 7 B-factor as a function of the Si content *x* as determined from the fit according to the Hendrickson-Bray approach.(24)

Although the *B* values could be defined only with one order of magnitude significance,(24) they reveal a clear tendency. With increasing content of Na^+ ions, *B* increases drastically by nine orders of magnitude as it is shown in Figure 7. This is consistent with the nature of *B* reflecting the linewidth changes caused by thermally activated Na^+ ions. The saturation of the structure with sodium ions slows down the Na^+ ions and also leads to the reduction of the average distance between them. This, in turn, increases the Na-Na dipolar couplings and the motion of the Na ions is not fast enough to suppress these interactions completely. As a result, the lines stay rather broad even at higher temperatures. This is especially pronounced for the sample $Na_{3.8}Sc_2(SiO_4)_{0.8}(PO_4)_{2.2}$ as can be seen from Figure 5b. Even at T = 523 K thermally activated ions still experience a significant degree of the dipolar interaction and higher temperatures are required to gain narrower lines.

3.2.2 T_1 relaxation studies of the Na^+-ion dynamics

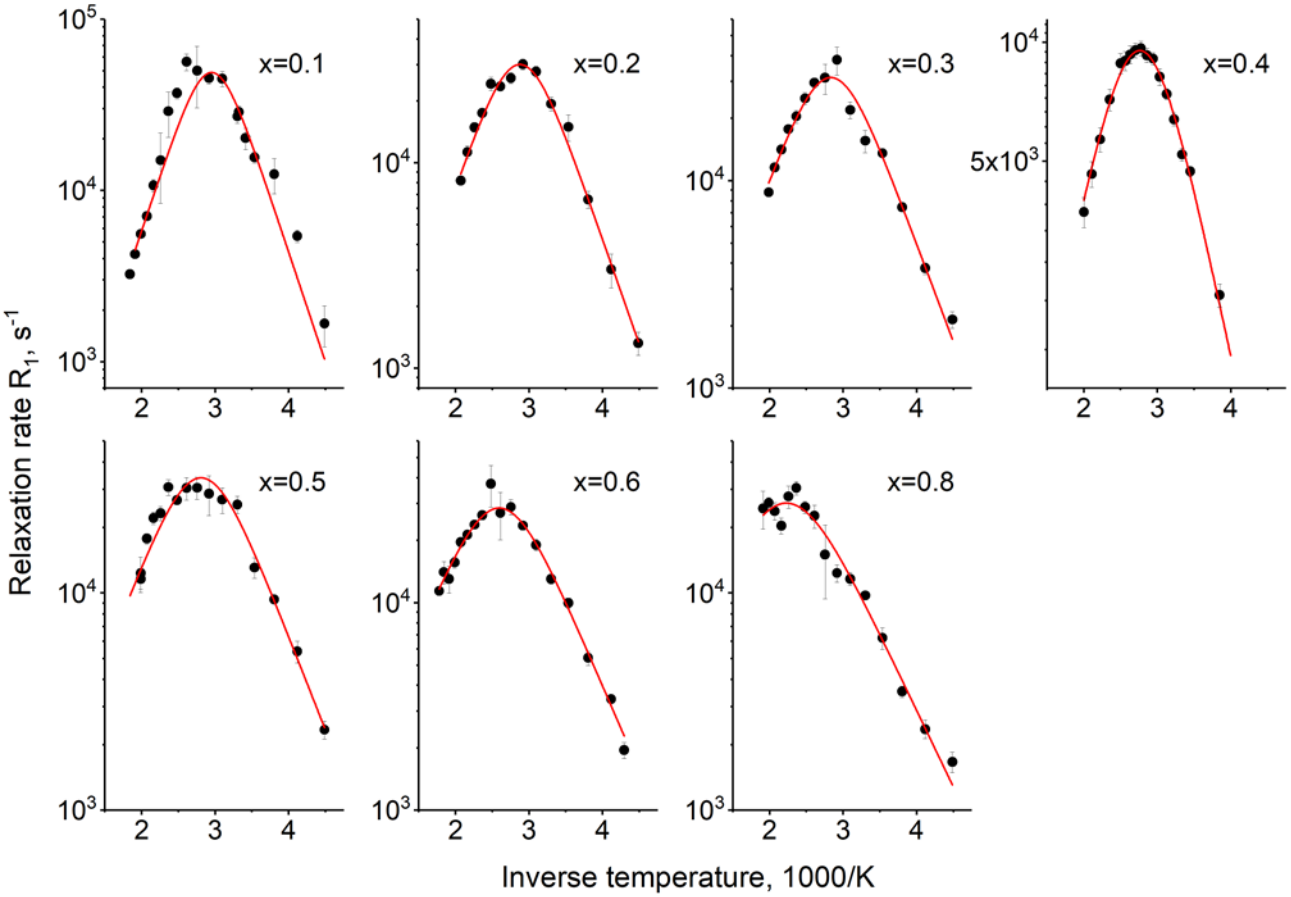

Figure 8 Temperature dependencies of the relaxation rates for different $NSSi_xP$ compositions. Black points indicate experimental results, whereas fitting curves are represented by red lines.

The analysis of the temperature dependence of ^{23}Na NMR relaxation rates $T_1^{-1}(T)$ complements the characterization of the ion dynamics and provides a more detailed picture of the local motions. It may reveal different processes with different characteristic time constants. The relaxation rate $R_1 = 1/T_1$ is proportional to the spectral density $J(\omega_0)$ of local field fluctuations at the Larmor frequency ω_0, according to the equation:

$$R_1 = \frac{1}{T_1} \sim J(\omega_0) \qquad \text{Equation 2}$$

In the simplest case, the spectral density is considered to be of the following form:(25)

$$J(\omega_0) \sim \frac{\tau_C}{1+(\omega_0\tau_C)^2} \qquad \text{Equation 3}$$

For a thermally activated process the correlation time τ_C , i.e. the average time the Na ions need to change their environment, can be described by an Arrhenius law:

$$\tau_C(T) = \tau_{298\,K} \cdot \exp\left(\frac{E_a}{k_B}\left(\frac{1}{T} - \frac{1}{298\,K}\right)\right) \qquad \text{Equation 4}$$

Here, $\tau_{298\,K}$ is the correlation time at room temperature, *T* is the temperature, k_B is the Boltzmann constant, and E_a is the activation energy. Combining equations 2-4, it is possible to extract the activation energy and the correlation time of the motion from the experimentally measured temperature dependence of the relaxation rates.

Figure 8 shows the temperature-dependent relaxation rates together with fitting curves according to the approach described above. The overall behavior for *x* = 0.1 to 0.5 looks very similar, i.e. the maximum of $T_1^{-1}(T)$ is located between 340 and 360 K. In contrast, for $NSSi_{0.6}P$ and $NSSi_{0.8}P$ the maximum is shifted towards higher temperatures, so that the high-temperature flank for *x* = 0.8 cannot be observed within the accessible temperature range. The

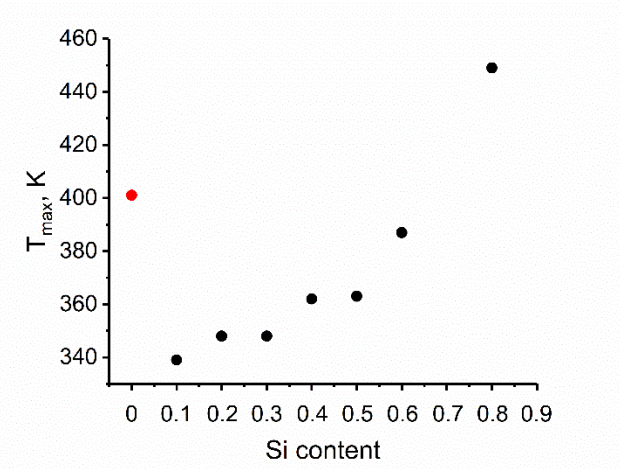

Figure 9 Temperature of the R_1 maximum for different Si contents *x*. The red point shows T_{max} of the monoclinic reference sample with *x* = 0.

temperatures where the maximum of T_1^{-1} is accessible are summarized in Figure 9. The temperature of the T_1^{-1} maximum for *x* = 0 (Fig. SI 3) is approximately at 400 K. However, the structure of this sample is different from that of the other samples and therefore a comparison of the ion dynamics is not straightforward. The monoclinic crystal structure results in a rather low ionic conductivity ($2.3 \cdot 10^{-5}$ S/cm at room temperature) for *x* = 0.

As obtained from the fitting procedure, the activation energy of the motion gradually decreases with increasing Si content (Figure 10). Although the absolute values for E_a are different, the overall trend resembles the one which was found from the motional narrowing analysis (see Table 1). The present set of materials includes one sample (x = 0.4) which was already characterised earlier with solid-state NMR relaxometry.(23) The small differences occurring in the current work in comparison to the results published earlier for this sample can be explained by the different ways that were used to analyse the data. While in our earlier work a single exponential was used to describe the magnetization transients, in the current work a stretched exponential was used to better describe the data. Nevertheless, the differences for both methods are small.

E_a and $\tau_{298\,K}$ are the main parameters which can be extracted from the experimentally measured relaxation rates. However, the diffusion coefficients and conductivity can better

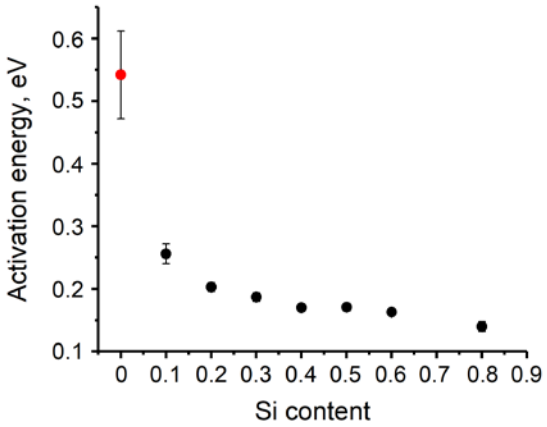

Figure 10 Activation energies derived from T_1 for different $NSSi_xP$ compositions. The red point denotes the monoclinic reference sample with x = 0.

visualize the motion of the ions inside the electrolytes. Combining temperature-dependent NMR data with XRD information and using the Einstein-Smoluchowkski equation (Eq. (5)) and Nernst-Einstein equation (Eq (6)), it is possible to estimate the ion mobility in $NSSi_xP$ electrolytes.

The diffusion coefficient D is proportional to the square of the average jump length l and the average jump rate of the motion $1/\tau_{298\,K}$:

$$D = f\frac{l^2}{2d}\tau_{298\mathrm{K}}^{-1}$$ Equation 5

Here, d denotes the dimensionality of the motion and f is the correlation factor, which is equal to 1 in case of a purely random motion and smaller than 1 for a correlated motion of the Na ions. For now, we assume an uncorrelated motion and use $f = 1$. From the diffusion coefficient *D* the Na^+ conductivity σ can be calculated via the Nernst-Einstein equation

$$\sigma = \frac{DNq^2}{k_{\mathrm{B}}T}$$ Equation 6

where N is the number density of Na^+ ions, q is the charge of the charge carriers, k_{B} denotes the Boltzmann constant, and T is the temperature. The conductivity pathway includes jumps between Na(1)-Na(2)/Na(3)-Na(1) sites.(4,5) The jump length and the unit cell volume were determined from XRD patterns with Rietveld refinement and are summarized in Table 2.

Table 2 Structural (XRD) and dynamical (T_1 studies) parameters (at 298 K) for $Na_{3+x}Sc_2(SiO_4)_x(PO_4)_{3-x}$: Shortest Na-Na distance l, unit cell volume *V*, diffusion coefficient D, and conductivity σ.

x	l, Å	V, Å^3 ($\Delta V = \pm 0.01$)	$D \cdot 10^{-12}$, m^2/s	σ, mS/cm
0.1	3.403	1541.43	1.93	1.45
0.2	3.4123	1546.70	2.08	1.61
0.3	3.4207	1549.20	2.12	1.69
0.4	3.4212	1551.85	2.01	1.65
0.5	3.4315	1552.62	2.16	1.82
0.6	3.4349	1553.68	1.5	1.31
0.8	3.4363	1554.06	1.05	0.96

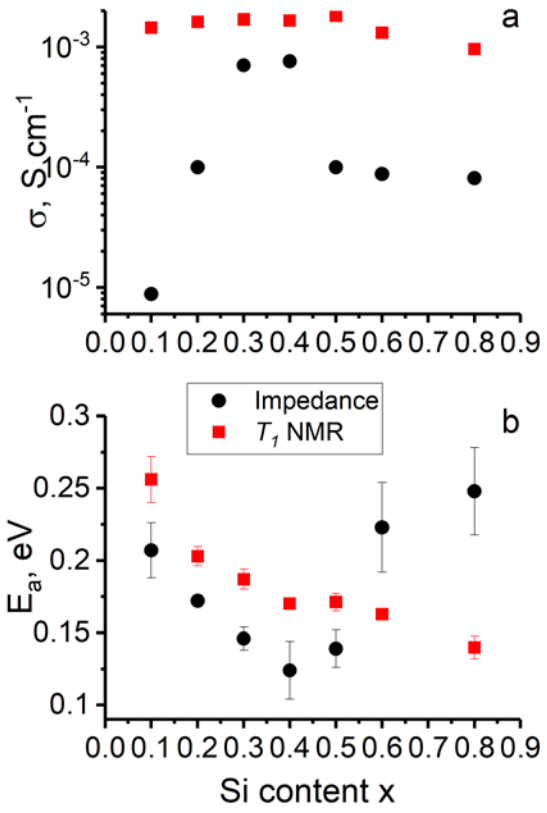

Figure 11 Ionic conductivities at 298 K (a) and activation energies (b) measured by NMR T_1 studies (red squares) and impedance spectroscopy (black circles). The conductivity data were determined from low-temperature impedance measurements between 283 and 243 K by extrapolation to 298 K.(4)

The diffusion coefficient *D* is almost constant in the range of silicon contents $0.1 < x < 0.5$. With further increasing of *x*, a decrease of *D* down to 1.1×10^{-12} m^2/s is observed. The calculated conductivity values reveal the same trend: a slight increase of σ ions at $x < 0.5$, corresponding to the increase of charge carriers, and then a decrease of the conductivity.

3.3 Comparison of local hopping observed by NMR relaxation times and long-range transport observed by impedance spectroscopy

Recently, the results of impedance measurements (IS) for this series of $NSSi_xP$ samples were reported.(4) The bulk conductivity could only be separated from the grain boundary conductivity at low temperatures. Above 283 K both contributions to the conductivity cannot be distinguished and only the total conductivity containing both bulk and grain-boundary

conductivity can be determined in the available frequency range. Nevertheless, due to the fact that the bulk and grain boundary conductivities depend on the temperature according to the Arrhenius law, measurements at lower temperatures allowed the estimation of the activation energies of both.(4)

The comparison between NMR-derived parameters and those from impedance spectroscopy is shown in Figure 11. T_1 relaxation data reflect the fast dynamics that correspond to the short-range motions on time scales of some nanoseconds. For a simple diffusion mechanism involving just a single type of jump process, the activation energies obtained from relaxation time studies should match the activation energies for the bulk conductivity. As we can see from the Figure 11 the activation energies from both techniques (blue symbols) are comparable in terms of absolute values. Moreover, the overall trend is similar in the range of $0.1 < x < 0.5$. The substitution of the PO_4 tetrahedra with SiO_4 changes the size of the unit cell due to the larger size of the SiO_4 groups. As a result, the bottleneck of the NASICON conductivity(4) becomes gradually larger. This facilitates Na(1)-Na(2) ionic jumps and lowers the activation energy. That is exactly the behavior observed in the T_1 relaxation data. An analogous dependence was reported for a larger number of NASICON materials. In that work(3) the activation energy of the ionic conductivity was plotted against the area of the T1 triangle.

The expansion of the unit cell is a continuous process. However, at $x>0.5$ the activation energy values derived from impedance spectroscopy significantly increase and the difference between NMR and impedance data becomes larger. The increase of the activation energy value was previously attributed(4) to the fact that the saturation of the structure with sodium ions increases with x. As a result, the deficiency of vacancies prevents random motion of Na^+. In other words, at low concentration of vacancies there is a high probability that after the first jump the Na ions return back to their previous position and such a forward-backward jump correlation does not contribute to the long-range transport. For the long-range displacement, multiple sodium ions would have to change their positions which requires higher energies, though the E_a value for a single jump still stays rather low.

As shown in Figure 11, the Si substitution leads to an increase of the conductivity until *x* reaches 0.5. Further increase of the Si content then lowers the diffusivity. This phenomenon is apparent from both the T_1 analysis and the results of impedance spectroscopy. The initial increase of the conductivity can result from the increasing amount of the charge carriers Na^+ and the enlargement of the T1 triangle which is a bottleneck for sodium conductivity in NASICON electrolytes. However, for high Si contents the amount of vacancies and available sites for the Na^+ ions are reduced and, thus, the diffusivity and the conductivity decreases.(2) As it was reported earlier for the similar series $Na_{1+x}Hf_2Si_xP_{3-x}O_{12}$(26) and for the Sc-containing $NSSi_xP$,(2,4) the optimum conductivity is reached when the amount of sodium ions per chemical formula is in the range of 3.2-3.4. The results of T_1 measurements are therefore in agreement with previous data and, as can be seen from Figure 11, the highest conductivity σ of 1.8 mS/cm corresponds to the composition $Na_{3.5}Sc_2(SiO_4)_{0.5}(PO_4)_{2.5}$.

The presence of correlated motions also explains the difference in conductivity values estimated from NMR and IS, as can be seen from Figure 11. In our relaxation time analysis, we assumed that the correlation factor *f* is equal to unity and the motion is purely random. In fact, even at *x*=0.1 the sodium sites are occupied by more than 40%(4) and this occupation results in more and more correlated jumps which is slowing down the long-range transport.

This means that the correlation factor *f* and the diffusion coefficient, as calculated from Eq. (5), would decrease with *x*.

In general, the existence of correlated motions is reflected in the shape of the T_1^{-1} relaxation curve as a function of inverse temperature. In this case the low-temperature (LT) and high-

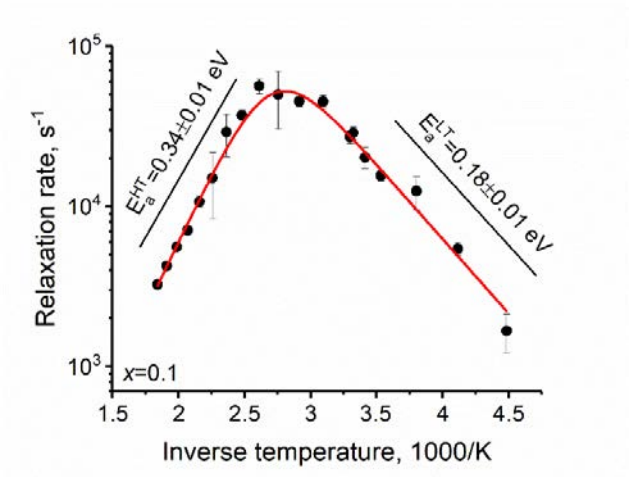

Figure 12 Asymmetric fitting according to Eq. (7) for the temperature-dependent relaxation rates of the NSSixP sample with x=0.1.

temperature (HT) flanks have different slopes,(27) which are characterised by activation energies E_a^{LT} and E_a^{HT} and the spectral density function has to be described by:

$$J(\omega_0) \sim \frac{\tau_C}{1+(\omega_0\tau_C)^{1+\beta}} \,. \qquad \text{Equation 7}$$

At least for the sample with *x*=0.1, the temperature dependence of R_1 can be better described with the asymmetric curve as shown in Figure 12. Then, the calculated conductivity extrapolated to 298 K gives a value of 0.55 mS/cm, which is closer to the value obtained from impedance data.

Recently, Deng et al.(28) also observed an asymmetric relaxation behavior in $Na_3Zr_2(SiO_4)_2(PO_4)$ and $Na_2Zr_2(SiO_4)_2(PO_4)_2$. In their work, they assigned the asymmetry to 2D-diffusion. It is worth noting that for 2D diffusion the HT-flank should have a smaller slope compared to the LT-flank.(23) In contrast, the HT-flank in Figure 12 is steeper, and thus the asymmetry cannot be ascribed to the low-dimensionality of motion in the current sample.

Summarizing the results of the relaxation studies, it is possible to conclude that with increasing *x* the activation energy of the local motions lowers. This effect is caused by the expansion of

the unit cell volume which facilitates ions to pass through the bottle-neck for the sodium mobility. This expansion occurs in the whole range of silicon contents *x*. A competitive process is the saturation of the unit cell with sodium ions, which leads to the reduction of the available vacancies. This lack of vacancies becomes more and more significant when *x* reaches and exceeds 0.5. This process is reflected in a decreasing ionic conductivity as measured by impedance spectroscopy and in the shift of the T_1^{-1}(T) maximum to higher temperatures observed with relaxation studies.

4. Conclusions

In the current work we used solid-state NMR spectroscopy to characterize the structure and local Na^+ ion mobility in a series of NASICON-type materials with chemical composition $Na_{3+x}Sc_2(SiO_4)_x(PO_4)_{3-x}$ ($0.1 < x < 0.8$). This series shows a high ionic conductivity at room temperature for all investigated Si contents *x*. The maximum in σ is reached at $x = 0.5$. At this value, the position of the maximum in the relaxation rate T_1^{-1}(T^{-1}) still remains at rather low temperatures indicating high local mobility of sodium ions at room temperature, and the activation barriers for such a local hopping becomes smaller and the jumps occur with higher probability.

If more P is substituted with Si, although the activation energy continues to slightly decrease, the room temperature mobility decreases, resulting in lower ionic conductivity. Such a behavior can be attributed to the saturation of the structure with sodium ions which occupy the formerly vacant sites, thereby increasing the correlations in subsequent Na jumps. These correltaions result in still quite fast local hopping but a decreasing long-range transport. This is also indicated by the highly sloping behaviour observed in the motional narrowing of the static ^{23}Na NMR spectra for large *x* that indicates that a significant amount of the Na ions is immobilized.

Overall, the results from NMR relaxation time studies, being sensitive to local hopping, confirm the results from impedance spectroscopy which is sensitive to the long-range transport of

charge carriers. $Na_{3.3}Sc_2(SiO_4)_{0.3}(PO_4)_{2.7}$ to $Na_{3.5}Sc_2(SiO_4)_{0.5}(PO_4)_{2.5}$ are the most promising materials for future application in all-solid-state Na-ion batteries.

References

1. S. Naqash, Q. Ma, F. Tietz and O. Guillon, $Na_3Zr_2(SiO_4)_2(PO_4)$ prepared by a solution-assisted solid state reaction, *Solid State Ionics*, 2017, **302**, 83–91.

2. Q. Ma, M. Guin, S. Naqash, C. L. Tsai, F. Tietz and O. Guillon, Scandium-substituted $Na_3Zr_2(SiO_4)_2(PO_4)$ prepared by a solution-assisted solid-state reaction method as sodium-ion conductors, *Chem. Mater.*, 2016, **28**, 4821–4828.

3. M. Guin and F. Tietz, Survey of the transport properties of sodium superionic conductor materials for use in sodium batteries, *J. Power Sources*, 2015, **273**, 1056–1064.

4. M. Guin, F. Tietz and O. Guillon, New promising NASICON material as solid electrolyte for sodium-ion batteries: Correlation between composition, crystal structure and ionic conductivity of $Na_{3+x}Sc_2Si_xP_{3-x}O_{12}$, *Solid State Ionics*, 2016, **293**, 18–26.

5. M. Guin, E. Dashjav, C. M. N. Kumar, F. Tietz and O. Guillon, Investigation of crystal structure and ionic transport in a scandium-based NASICON material by neutron powder diffraction, *Solid State Sci.*, 2017, **67**, 30–36.

6. M. Guin, S. Indris, M. Kaus, H. Ehrenberg, F. Tietz and O. Guillon, Stability of NASICON materials against water and CO_2 uptake, *Solid State Ionics*, 2017, **302**, 102–106.

7. P. Heitjans and S. Indris, Diffusion and ionic conduction in nanocrystalline ceramics, *J. Phys. Condens. Matter.*, 2003, **15**, R1257–R1289.

8. R. Böhmer, K. R. Jeffrey and M. Vogel, Solid-state Li NMR with applications to the translational dynamics in ion conductors, *Prog. Nucl. Magn. Reson. Spectrosc.*, 2007, **50**, 87-174.

9. V. Petrícek, M. Dušek and L. Palatinus, Crystallographic computing system JANA2006: General features, *Z. Krist.*, 2014, **229**, 345–352.

10. G. Collin, R. Comes, J. P. Boilot and P. Colomban, Disorder of Tetrahedra in NASICON-Type Structure-I. $Na_3Sc_2(PO_4)_3$: Structure and Ion-Ion Correlations, *J. Phys.*

Chem. Solids 1986, **47**, 843–854.

11. M. Barj, H. Perthuis and P. Colomban, Relations between sublattice disorder, phase transitions and conductivity in NASICON, *Solid State Ionics*, 1983, **9–10**, 845–850.

12. M. Barj, G. Lucazeau and C. Delmas, Raman and infrared spectra of some chromium Nasicon-type materials: Short-range disorder characterization, *J. Solid State Chem.*, 1992, **100**, 141–150.

13. T. Furukawa, K. E. Fox and W. B. White, Raman spectroscopic investigation of the structure of silicate glasses. III. Raman intensities and structural units in sodium silicate glasses, *J. Chem. Phys.*, 1981, **75**, 3226.

14. B. O. Mysen, L. W. Finger, D. Virgo and F. A. Seifert, Curve-fitting of Raman spectra of silicate glasses, *Am. Mineral.*, 1982, **67**, 686–95.

15. S. Difi, I. Saadoune, M. T. Sougrati, R. Hakkou, K. Edstrom and P. E. Lippens, Mechanisms and Performances of $Na_{1.5}Fe_{0.5}Ti_{1.5}(PO_4)_3$/C Composite as Electrode Material for Na-Ion Batteries, *J. Phys. Chem. C*, 2015, **119**, 25220–25234.

16. P. K. Jha, O. P. Pandey and K. Singh, Optimization of High Conducting $Na_3Zr_2Si_2PO_{12}$ Phase by new Phosphate Salt for Solid Electrolyte, *Silicon*, 2017, **9**, 411–419.

17. K. J. Rao, K. C. Sobha and S. Kumar, Infrared and Raman spectroscopic studies of glasses with NASICON-type chemistry, *Proc. Indian Acad. Sci.*, 2001, **113**, 497–514.

18. R. Tabeta and H.Saito, ^{23}Na Chemical shifts of some inorganic and organic compounds in the solid state as determined by the magic angle spinning and high power NMR method, *Chem. Lett.*, 1984, **2**, 293–296.

19. R. Morita, K. Gotoh, M. Fukunishi, K. Kubota, S. Komaba, N. Nishimura, T. Yumura, K. Deguchi, S. Ohki, T. Shimizu and H. Ishida, Combination of solid state NMR and DFT calculation to elucidate the state of sodium in hard carbon electrodes, *J. Mater. Chem. A.*, 2016, **4**, 13183–13193.

20. G. Wu, An approximate analytical expression for the nuclear quadrupolar transverse relaxation rate of half-integer spins in liquids, *J. Magn. Reson.*, 2016, **269**, 176-178.

21. J. Shen, V. Terskikh and G. Wu, Observation of the Second-Order Quadrupolar

Interaction as a Dominating NMR Relaxation Mechanism in Liquids: The Ultraslow Regime of Motion, *J. Phys. Chem. Lett.*, 2016, **7**, 3412-3418.

22. C. Jäger, G. Scheler, U. Sternberg, S. Barth and A. Feltz, ^{29}Si and ^{31}P MAS NMR Study of the NASICON System $Na_{1+x}Zr_2(SiO_4)_x(PO_4)_{3-x}$, *Chem. Phys. Lett.*, 1988, **147**, 49–52.

23. M. Kaus, M. Guin, M. Yavuz, M. Knapp, F. Tietz, O. Guillon, et al., Fast Na^+ Ion Conduction in NASICON-Type $Na_{3.4}Sc_2(SiO_4)_{0.4}(PO_4)_{2.6}$ Observed by $_{23}$Na NMR Relaxometry, *J. Phys. Chem. C*, 2017, **121**, 1449-1454.

24. J. R. Hendrickson and P. J. Bray, A phenomenological equation for NMR motional narrowing in solids, *J. Magn. Reson.*, 1973, **9**, 341–357.

25. N. Bloembergen, E. M. Purcell and R. V. Pound, Relaxation effects in nuclear magnetic resonance absorption, *Phys. Rev.*, 1948, **73**, 679–712.

26. E. M. Vogel, R. J. Cava and E. Rietman, Na^+ ion conductivity and crystallographic cell characterization in the Hf-NASICON system $Na_{1+x}Hf_2Si_xP_{3-x}O_{12}$, *Solid State Ionics*, 1984, **14**, 1–6.

27. P. Heitjans, A. Schirmer and S. Indris, NMR and β-NMR studies of diffusion in interface-dominated and disordered solids. In: Diffusion in Condensed Matter: Methods, Materials, Models. Springer, Berlin, 2005. p. 367-415.

28. Y. Deng, C. Eames, L. H. B. Nguyen, O. Pecher, K. J. Griffith, M. Courty, B. Fleutot, J. N. Chotard, C. P. Grey, M. S. Islam and C. Masquelier C, Crystal structures, local atomic environments and ion diffusion mechanisms of scandium-substituted sodium superionic conductor (NASICON) solid electrolytes, *Chem. Mater.*, 2018, **30**, 2618–2630.